Three-dimensional seismic tomography from P wave and S wave microearthquake travel times and rock physics characterization of the Campi Flegrei Caldera

T. Vanorio, J. Virieux, P. Capuano, G. Russo

Three-dimensional seismic tomography from *P* wave and *S* wave microearthquake travel times and rock physics characterization of the Campi Flegrei Caldera

T. Vanorio and J. Virieux
UMR-Geosciences Azur, CNRS, Université de Nice, Sophia Antipolis, France

P. Capuano
Dipartimento di Scienze e Tecnologie per l'Ambiente ed il Territorial, Università del Moliere, Isernia, Italy

G. Russo
Dipartimento di Scienze Fisiche, Università di Napoli, Naples, Italy

Received 22 March 2004; revised 5 November 2004; accepted 10 December 2004; published 1 March 2005.

[1] The Campi Flegrei (CF) Caldera experiences dramatic ground deformations unsurpassed anywhere in the world. The source responsible for this phenomenon is still debated. With the aim of exploring the structure of the caldera as well as the role of hydrothermal fluids on velocity changes, a multidisciplinary approach dealing with three-dimensional delay time tomography and rock physics characterization has been followed. Selected seismic data were modeled by using a tomographic method based on an accurate finite difference travel time computation which simultaneously inverts *P* wave and *S* wave first-arrival times for both velocity model parameters and hypocenter locations. The retrieved *P* wave and *S* wave velocity images as well as the deduced V_p/V_s images were interpreted by using experimental measurements of rock physical properties on CF samples to take into account steam/water phase transition mechanisms affecting *P* wave and *S* wave velocities. Also, modeling of petrophysical properties for site-relevant rocks constrains the role of overpressured fluids on velocity. A flat and low V_p/V_s anomaly lies at 4 km depth under the city of Pozzuoli. Earthquakes are located at the top of this anomaly. This anomaly implies the presence of fractured overpressured gas-bearing formations and excludes the presence of melted rocks. At shallow depth, a high V_p/V_s anomaly located at 1 km suggests the presence of rocks containing fluids in the liquid phase. Finally, maps of the V_p*V_s product show a high V_p*V_s horseshoe-shaped anomaly located at 2 km depth. It is consistent with gravity data and well data and might constitute the on-land remainder of the caldera rim, detected below sea level by tomography using active source seismic data.

Citation: Vanorio, T., J. Virieux, P. Capuano, and G. Russo (2005), Three-dimensional seismic tomography from *P* wave and *S* wave microearthquake travel times and rock physics characterization of the Campi Flegrei Caldera, *J. Geophys. Res.*, *110*, B03201, doi:10.1029/2004JB003102.

1. Introduction

[2] The CF Caldera, located to the west of the city of Naples, is one of the active volcanic systems of Southern Italy. Several eruptions have occurred during historical times characterizing the structure of this caldera by sparse volcanic craters. However, two explosive events have mainly affected its volcanic structure: the Campanian Ignimbrite and the Neapolitan Yellow tuff eruption [*Scandone et al.*, 1991].

[3] As with many calderas, CF periodically experiences notable unrest episodes which include ground deformations, seismic swarms and increases in the degassing activity [*Barberi et al.*, 1984]. However, unlike other calderas, ground deformations in CF may reach values unsurpassed anywhere in the world [*Newhall and Dzurisin*, 1988]. On the basis of historical records, the uplift phase may precede a new eruptive event as occurred in 1538 when a vertical displacement of 7 m preceded the eruption of Mount Nuovo [*Dvorak and Gasparini*, 1991]. Nevertheless, short uplift phases may also interrupt the secular subsidence as occurred in 1970–1972, 1982–1984, 1989, 1994 and, 2000 without culminating in an eruption. The crisis in 1982–1984 was particularly dramatic when an impending eruption was feared as more than 15,000 shallow earthquakes having maximum magnitude of 4.0 occurred and uplift rates of 3 mm/d were observed [*Aster and Meyer*, 1988] which brought a total vertical displacement of 1.8 m [*Barberi et al.*, 1984; *Osservatorio Vesuviano*, 1985]. By January 1985, seismic

0148-0227/05/2004JB003102$09.00

activity strongly dropped and slow subsidence began. To date, about 70 cm of the 1982–1984 total uplift has been removed by subsidence.

[4] Mechanisms accounting for these phenomena have generally involved pressure generation exerted either from a magma chamber [*Bianchi et al.*, 1987; *Dzurisin and Yamashita*, 1987; *Bonafede et al.*, 1986] or from hydrothermal reservoirs [*Oliveri del Castillo and Quagliariello*, 1969; *Casertano et al.*, 1976; *Bonafede*, 1991; *De Natale et al.*, 1991; *Gaeta et al.*, 1998]. Nevertheless, modeling of ground deformation data shows that any of the possible sources responsible for the recurrent uplift and subsidence has to be placed between 1.5 to 4 km depth, in order to fit both the magnitude and the narrow bell shape of the recorded displacement [*Bianchi et al.*, 1987; *Bonafede*, 1991; *De Natale et al.*, 1991; *Gaeta et al.*, 1998].

[5] The presence of a magmatic reservoir underneath the CF Caldera has been proposed as a possible interpretation of both *P-S* converted phases at 4 km depth [*Ferrucci et al.*, 1992] and temperature data inferred by Q_p models [*De Lorenzo et al.*, 2001]. However, no evidence for magma bodies having volumes larger than 1 km^3 has been found down to 4–5 km by the recent three-dimensional (3-D) *P* wave tomography performed in the Gulf of Naples and Pozzuoli [*Zollo et al.*, 2003]. Furthermore, no variation of isotopic ratios of magma-derived species has been found in fumaroles during the 1982–1984 unrest that could serve as evidence for the magmatic origin of the crisis [*Tedesco et al.*, 1990; *Allard et al.*, 1991].

[6] The possibility that hydrothermal fluids play a fundamental role in triggering activity at CF often attracts attention because a correlation between ground displacement and gas emission rate has been found [*Barberi et al.*, 1984; *Chiodini et al.*, 2003]. Nevertheless, signatures indicating caprock formations, which are required to build up pore fluid pressure within reservoirs, have not yet been detected. Under the hypothesis of pore fluid pressure generation, the assessment of caprock formations constitutes evidence constraining the depth of the triggering source. Thus many questions still remain unresolved and mechanisms responsible for the CF activity not well constrained.

[7] Local earthquake tomography constitutes a basic tool to assess the 3-D velocity structure in seismically active areas [*Thurber*, 1992]. In order to investigate the structure of the caldera, its earthquake distribution, and the role of hydrothermal fluids, a multidisciplinary study involving 3-D delay time tomography of *P* and *S* microearthquake travel times and rock physics characterization is presented in this paper.

[8] In the CF area, a previous joint tomographic and earthquake location study using microearthquake travel times was performed by *Aster and Meyer* [1988], who used 228 events occurring during the 1982–1984 crisis. They reported both a high V_p/V_s ratio at 1 km depth that was interpreted as a region of highly water saturated fractured rocks and a cessation of seismicity at approximately 4 km.

[9] In the new seismic tomographic study reported in this paper, we repicked and upgraded the 1982–1984 data set by largely increasing the number of *P* wave and *S* wave time readings compared to the previous study [*Aster and Meyer*, 1988]. The assessment of a reliable *S* wave velocity structure is crucial, especially in a geothermal field, to overcome ambiguities deriving from the interpretation of the *P* wave velocity field alone. To improve the interpretation of the retrieved anomalies, we also investigated the role of hydrothermal fluids on *P* wave and *S* wave velocities via effective medium modeling. Both laboratory measurements on site-relevant lithologies under controlled conditions of pressure [*Vanorio et al.*, 2002; *Vanorio*, 2003] and the comparison with those made on other lithologies under pressure and temperature conditions [*Ito et al.*, 1979; *Wang and Nur*, 1989] constrained the modeling results.

[10] The combined approach afforded in this study brings new clues useful to assessing the CF Caldera structure and, in turn, its activity.

2. Network and Data Selection

[11] To monitor the seismic activity accompanying the 1982–1984 crisis, the University of Wisconsin began a field experiment deploying a temporary network consisting of 21 three-component digital short-period seismometers (WS). This network complemented those maintained by the Vesuvian Observatory (VO) and Agip (Azienda Generale Italiana Petroli, AG) consisting of 25 analog vertical seismic stations (Figure 1). Data were recorded at 100- or 200-Hz sampling rates and 1-Hz geophones were used [*Aster and Meyer*, 1988]. More than 15,000 events were recorded by the seismic monitoring network. Events were clustered in time, mainly concentrated in the Pozzuoli-Solfatara area and had maximum duration magnitudes $M_d \leq 4$ [*De Natale and Zollo*, 1986].

[12] In the frame of the so-called SERAPIS project, most of the waveforms recorded by the digital network were recovered and picked by the different participating groups. However, an analysis of the manually picked times showed that a more homogeneous repicking was required for a detailed seismic imaging. Consequently, we repicked the whole SERAPIS database. Furthermore, we added the data collected by the permanent network. This work has significantly augmented the data set used in *Aster and Meyer*'s [1988] study.

[13] We used a subdata set consisting of 1209 microearthquakes occurring from 1 January through 15 April 1984 which provided 7264 *P* and 3121 *S* arrival time readings. Arrival times measured from digitized seismograms were estimated to be accurate in the range of 0.02–0.05 s for *P* and 0.02–0.1 s for *S* waves. A preliminary hypocenter location was determined by using the 1-D *P* velocity model resulting from the active seismic experiment performed in the Bay of Pozzuoli [*Zollo et al.*, 2003]. From the initial data set, we selected earthquakes that had at least 6 *P* and 4 *S* phases read, azimuthal gaps smaller than 180°, and RMS time residuals smaller than 0.5 s. This selection provided a database consisting of 462 events with a final number of *P* and *S* readings of 3447 and 2289, respectively.

3. Tomographic Inversion Procedure

[14] We used a linearized, iterative tomographic approach as proposed by many authors [e.g., *Spakman and Nolet*, 1988; *Aster and Meyer*, 1988; *Hole et al.*, 2000; *Benz et al.*, 1996; *Le Meur et al.*, 1997; *Latorre et al.*, 2004] in which *P*

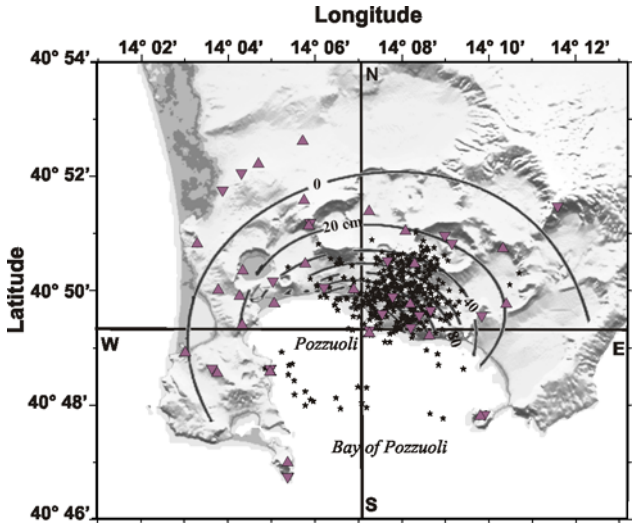

Figure 1. Map of the Campi Flegrei Caldera showing seismometer stations (inverted triangles, WS network; triangles, VO and AG networks) and final earthquake locations (black stars). The map also shows the elevation contours (black lines) for the 1982–1984 uplift.

and *S* first arrival times are simultaneously inverted for both earthquake locations and velocity model parameters at each step of the inversion procedure. The importance of coupling earthquake hypocenter parameters (locations and origin time) on the one hand and velocities on the other has been discussed by *Thurber* [1992], who emphasized that all required parameters should be mutually consistent to avoid significant bias in the derived models.

[15] The distribution of stations/events allowed us to investigate a model volume of $14 \times 14 \times 7$ km^3 with the top at 0.5 km above sea level. Assessing the most suitable model parametrization in seismic tomography is an important task since it controls the final solution as well as its reliability. By using synthetic data, different grid spacings were tested to check for the most appropriate model parametrization and to avoid the introduction of artifacts and false anomalies. For the same purpose, model results obtained by shifting the grid were also tested. Trial tests demonstrated that a uniform grid spacing at the size of $0.5 \times 0.5 \times 0.5$ km^3 allow us to fairly well delineate the main retrieved anomalies, and so it represents the best compromise among model parameterization, spatial resolution, and a reliable representation of the velocity field.

[16] First arrival travel times of wave fronts are computed through a finite difference solution of the eikonal equation [*Podvin and Lecomte*, 1991] in a finer grid of $0.1 \times 0.1 \times 0.1$ km^3. The latter consists of constant slowness cells computed by trilinear interpolation from the inversion grid. For each event-receiver pair, travel times are recalculated by numerical integration of the slowness field along the previously traced rays. *Latorre et al.* [2004] demonstrated that travel times computed in this way are more precise than those computed by wave front construction and thus they are less sensitive to the grid spacing used for the forward problem. Travel time partial derivatives are simultaneously computed for *P* wave and *S* wave slowness fields, hypocenter location, and origin time. These parameters are inverted simultaneously without any parameter separation technique [*Pavlis and Booker*, 1980; *Spencer and Gubbins*, 1980] by using the LSQR algorithm [*Paige and Saunders*, 1982]. As described by *Benz et al.* [1996], smoothness constraint equations based on second derivatives are used to control the degree of model roughness (i.e., the degree of variation in slowness) allowed during the inversion procedure by the requirement that the Laplacian of the slowness field must vanish [*Menke*, 1984].

3.1. The 1-D Model Selection

[17] Inherently, in a linearized tomographic approach, velocity perturbations cannot move too far from the unperturbed model. As a consequence, the final solution will depend strongly on the a priori choice of the 1-D reference model [*Kissling et al.*, 1994]. As a first approach, we used the 1-D *P* wave velocity model resulting from the tomographic inversion of 77,000 first *P* wave arrival times collected during the active seismic experiment performed in the CF Caldera [*Zollo et al.*, 2003]. The initial *S* velocity model was derived from the *P* velocity model using a V_p/V_s ratio of 1.7 estimated from Wadati diagrams [*Lay and Wallace*, 1995]. However, we verified the agreement between the initial 1-D velocity model [*Zollo et al.*, 2003] and earthquake data because of both the inherent difference in the geometry of the passive and active experiments and the elapsed time between the acquisition of the two data sets ($\sim$20 years). The latter is a significant factor due to the changes occurring in geothermal systems.

[18] A statistical study of the final 3-D solution was inferred from 400 initial 1-D models, randomly generated within two extreme 1-D velocity bounds (Figure 2a, gray solid lines). The upper and lower velocity bounds were chosen to have the 1-D reference model of *Zollo et al.* [2003] as average (Figure 2a, cyano dashed line). Figure 2a shows that even though different initial models provided substantially unlike RMS time residuals, the data misfit of all final solutions reached about the same value (close to $\sim$0.08 s). A similar result is obtained using the reference model (Figure 2a, cyano star). Also, the RMS time residuals (Figure 2a, black circles) associated with the 400 initial 1-D velocity models fall into two ranges. The first one includes values smaller than 0.2 s while the second higher than 0.2 s. Note that the initial value of RMS residuals resulting from the reference 1-D velocity model falls in the range of values greater than 0.2 s (cyano star). In addition, the initial distribution of time residuals associated with the *P* and *S* reference models and earthquake locations (Figure 3a, gray histogram) is shifted toward positive values compared to the distribution associated with the final solution (Figure 3a, black histogram). Such a shift indicates an overestimation of the reference 1-D velocity model which could affect velocity estimates in the final models.

[19] On account of the above considerations, we made a more restrictive selection on the 1-D reference model. We have chosen as a reference the average velocity model resulting from those associated with RMS residuals $\leq$0.2 s (Figure 2b, red dashed line). This selection provided a lower RMS of the final 3-D solution (0.07 s) (Figure 2b, lower red star), a reduction of 46% from the initial RMS value of 0.13

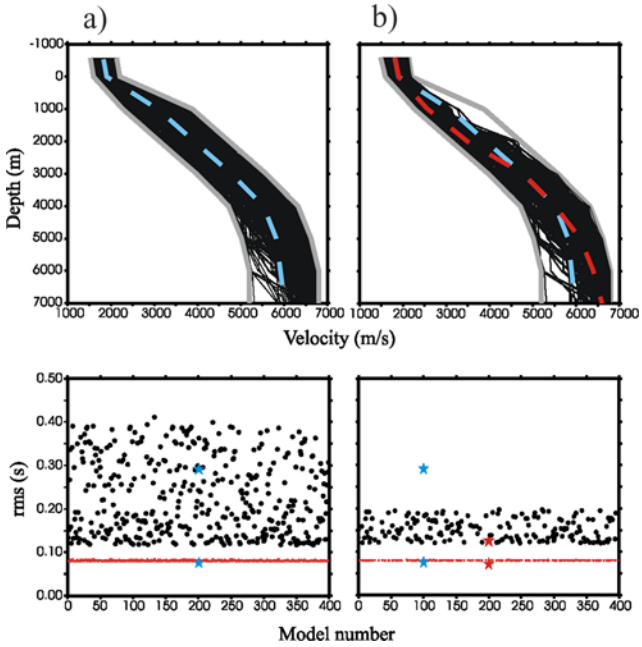

Figure 2. (a) Randomly generated initial 1-D velocity models. The upper and lower velocity bounds (solid gray lines) and the 1-D velocity model from *Zollo et al.* [2003] (dashed cyano line) are also shown. (bottom left) Initial (black points) and final misfit values (red points) obtained from inversions. Cyano stars indicate the initial and the final misfit values for the 1-D velocity model of *Zollo et al.* [2003]. (b) Same as Figure 2a, after the selection described in the text.

Figure 2b, upper red star, and a zero-centered distribution of travel time residuals (Figure 3b).

4. Tomographic Inversion Result

4.1. Three-Dimensional *P* and *S* Velocity Models and Earthquake Locations

[20] *P* wave and *S* wave velocity structures and earthquake locations are shown in Figures 4a and 4b. Cells not sampled by any ray are shown in gray. Down to 4 km depth, both the V_p/V_s images show (1) a low-velocity anomaly within the inner part which ranges from 1.7 to 3.8 km/s for *P* wave velocity and from 1.0 to 2.5 km/s for *S* wave velocity and (2) a surrounding annular high-velocity anomaly ($\geq$4.8 km/s for *P* wave velocity and $\geq$2.8 km/s for *S* wave velocity). Beyond 4 km depth, the inner low-velocity anomaly still appears in the V_p structure, while it is less evident in the V_s field. In order to determine possible lithological variations at depth or zones with different porosities and/or crack densities, maps showing the V_p*V_s products were deduced from the retrieved *P* wave and *S* wave velocity images. Both lithology and porosity affect *P* wave and *S* wave velocities while fluid saturation only affects *P* wave velocity. Therefore V_p*V_s mapping allows us to highlight anomalies that are caused by either lithology or porosity and at the same time to minimize those related to fluid saturation. The V_p*V_s image shown in Figure 4c, highlights a horseshoe-shaped high V_p*V_s anomaly at 2 km depth. *Zollo et al.* [2003] have reported a fairly good match between the arc shaped high *P* wave velocity anomaly inferred from active source 3-D seismic tomography and the positive annular gravity anomaly characterizing the CF Caldera [*Capuano and Achauer*, 2003]. *Zollo et al.* [2003] correlated the high *P* velocity anomaly detected in the Bay of Pozzuoli to the buried caldera rim. The high V_p*V_s anomaly reported in this study is consistent with the onshore positive gravity anomaly inferred by *Capuano and Achauer* [2003] and might constitute the remaining part of the caldera rim detected below sea level by active source tomography [*Zollo et al.*, 2003].

[21] Figures 5a and 5b show *P* wave and *S* wave velocity vertical cross sections along the E-W and N-S directions shown in Figure 1. Along both directions, a high-velocity structure having a concave shape characterizes the deeper part of the caldera. On the other hand, at shallower depths, lower velocities mark its inner portion. Earthquakes mostly cluster in the inner part of the velocity structure defining a narrow easterly trend (northeasterly on map views) which extends from near the surface (ACC, Accademia, and W12, Solfatara A) to ~4.0 km depth. At greater depths, earthquakes are distributed along the borders of the high-velocity structure (Figures 4a and 4b).

4.2. Velocity Model Resolution

[22] To verify the spatial resolution of the inferred 3-D models, synthetic tests on a global scale (e.g., standard checkerboard tests) as well as on a local scale (e.g., spike tests) were performed. A sinusoidal function having a wavelength of 1 km in all directions (*x*, *y*, and *z*) and an amplitude of ±0.1 km/s for *P* velocity and of ±0.15 km/s for *S* velocity was added to the final tomographic models. By

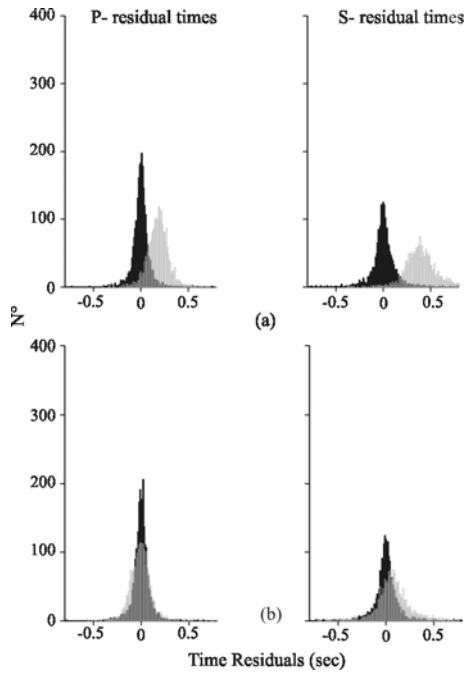

Figure 3. Initial (gray) and final (black) distribution of travel time residuals for *P* wave and *S* wave velocity models by using (a) the 1-D velocity model from *Zollo et al.* [2003] and (b) the 1-D model obtained after our restrictive selection of resulting RMS.

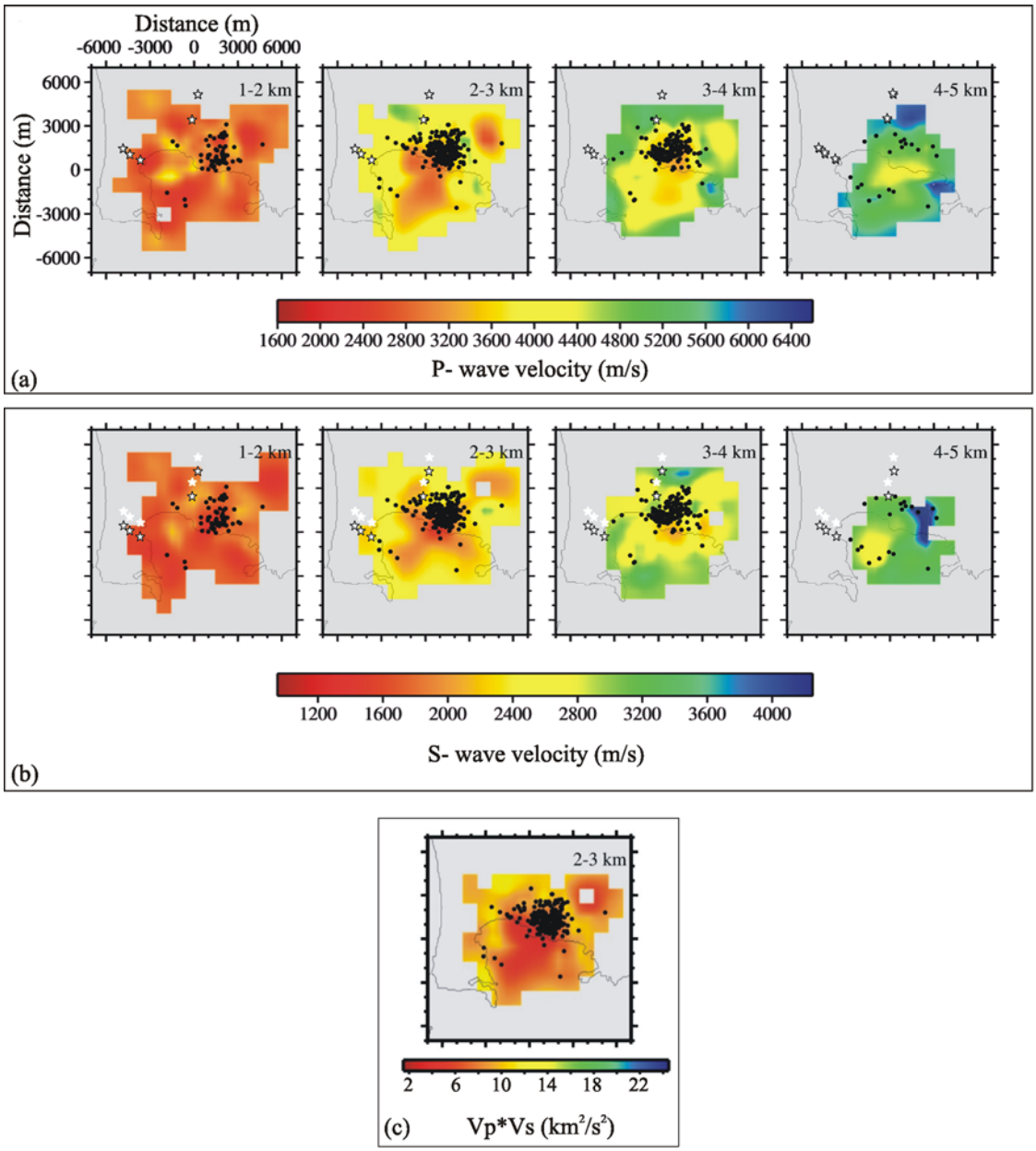

Figure 4. Map views showing the final solutions for (a) *P* wave and (b) *S* wave velocity structures. Black circles and black stars indicate earthquake and well locations. (c) Map view showing the V_p*V_s product at 2.5 km depth.

fixing earthquake locations, the computed travel times were inverted for *P* wave and *S* wave velocity parameters.

[23] Test results show (Figures 6a and 6b) that anomalies having wavelengths of 1 km are fairly well reproduced in the whole area down to 6 km depth while, due to the ray path geometry, poorer resolution is found in the bay.

[24] We also checked the resolution of our final models in specific areas by performing several spike resolution tests which represent a numerical way for estimating the resolution matrix. The area of interest is located between the Accademia (ACC station) and Solfatara areas (W02 and W12 stations) and the resolution of a spike anomaly placed at 4 km depth was analyzed. Tests were carried out by adding both positive and negative anomalies to the final *P* wave and *S* wave models. The inversion of the computed travel times for model parameters was made by following the same procedure as for the checkerboard tests. Figures 7a and 7b show a map view of the recovered *P* wave and *S* wave velocity anomalies as well as their variation as a function of depth both for positive (Figure 7a) and negative anomalies (Figure 7b). Results of spike tests demonstrate that size and amplitude of both positive and negative anomalies placed at 4 km depth can be fairly well resolved in this region.

4.3. Velocity Model Uncertainty

[25] As described in previous sections, many factors affect the final result of a tomographic inversion proce-

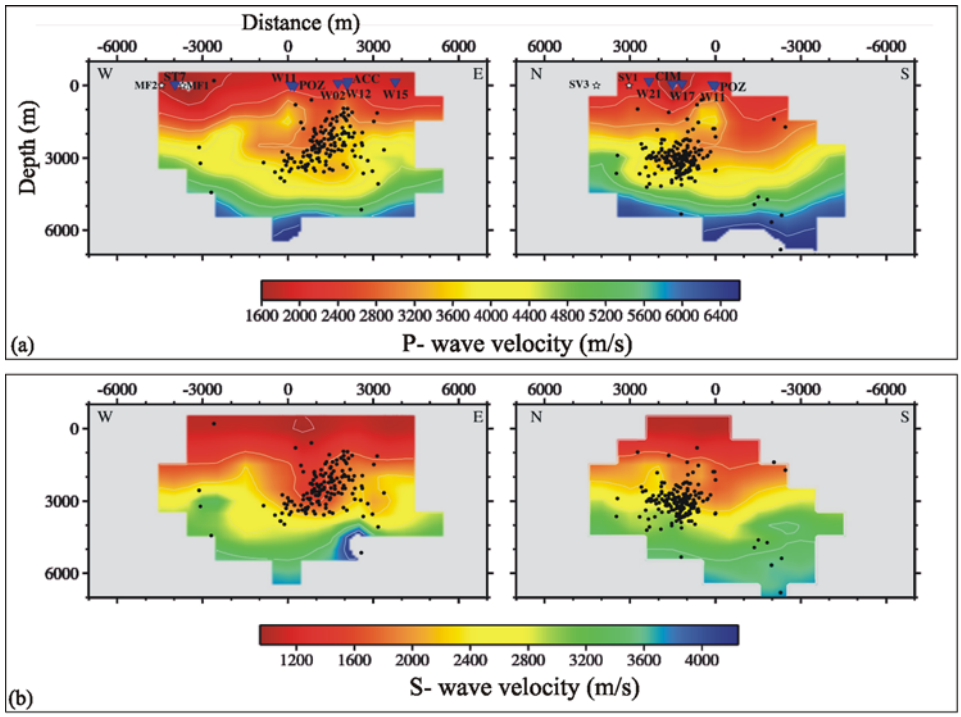

Figure 5. Vertical cross sections for (a) *P* and (b) *S* velocity models along the W-E and N-S directions reported in Figure 1. Black circles, black stars, and triangles indicate earthquake, well, and station locations.

dure such as the coupling between the earthquake hypocenters and the velocity parameters [*Thurber*, 1992], the initial 1-D velocity model [*Kissling et al.*, 1994], as well as the size of the grid used for data inversion and the regularization technique. Similarly, the source-station geometry which in turn affects ray path distribution is a critical factor in resolving velocity structure. In order to estimate if our distribution of earthquake hypocenters and

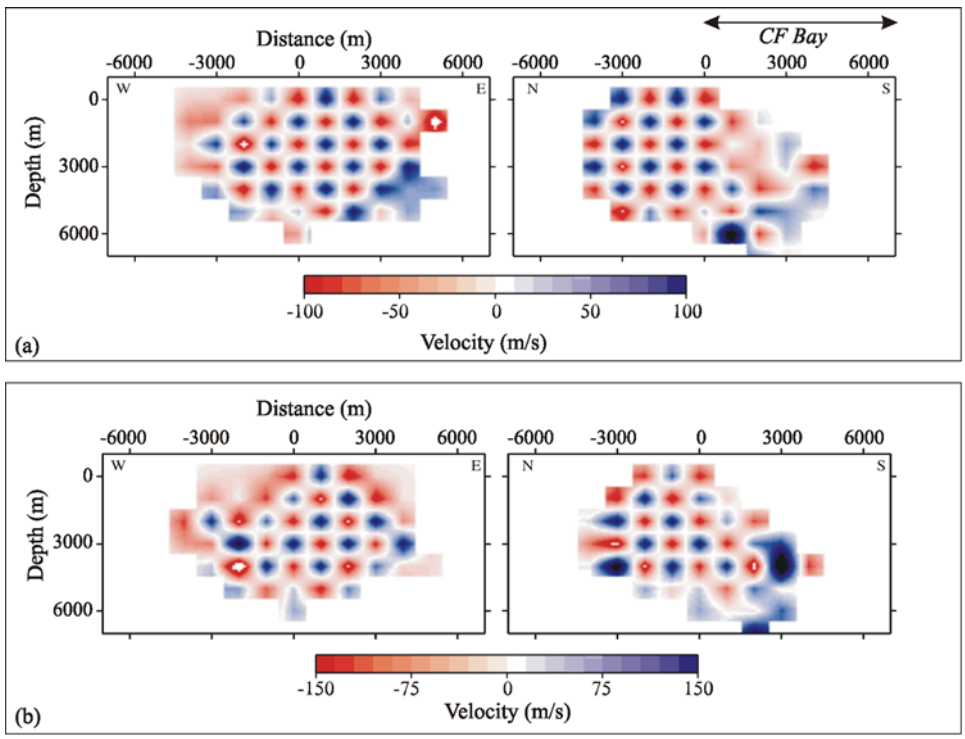

Figure 6. Vertical cross sections along the W-E and N-S directions of the checkerboard model perturbations after inversion for (a) the *P* and (b) *S* velocity.

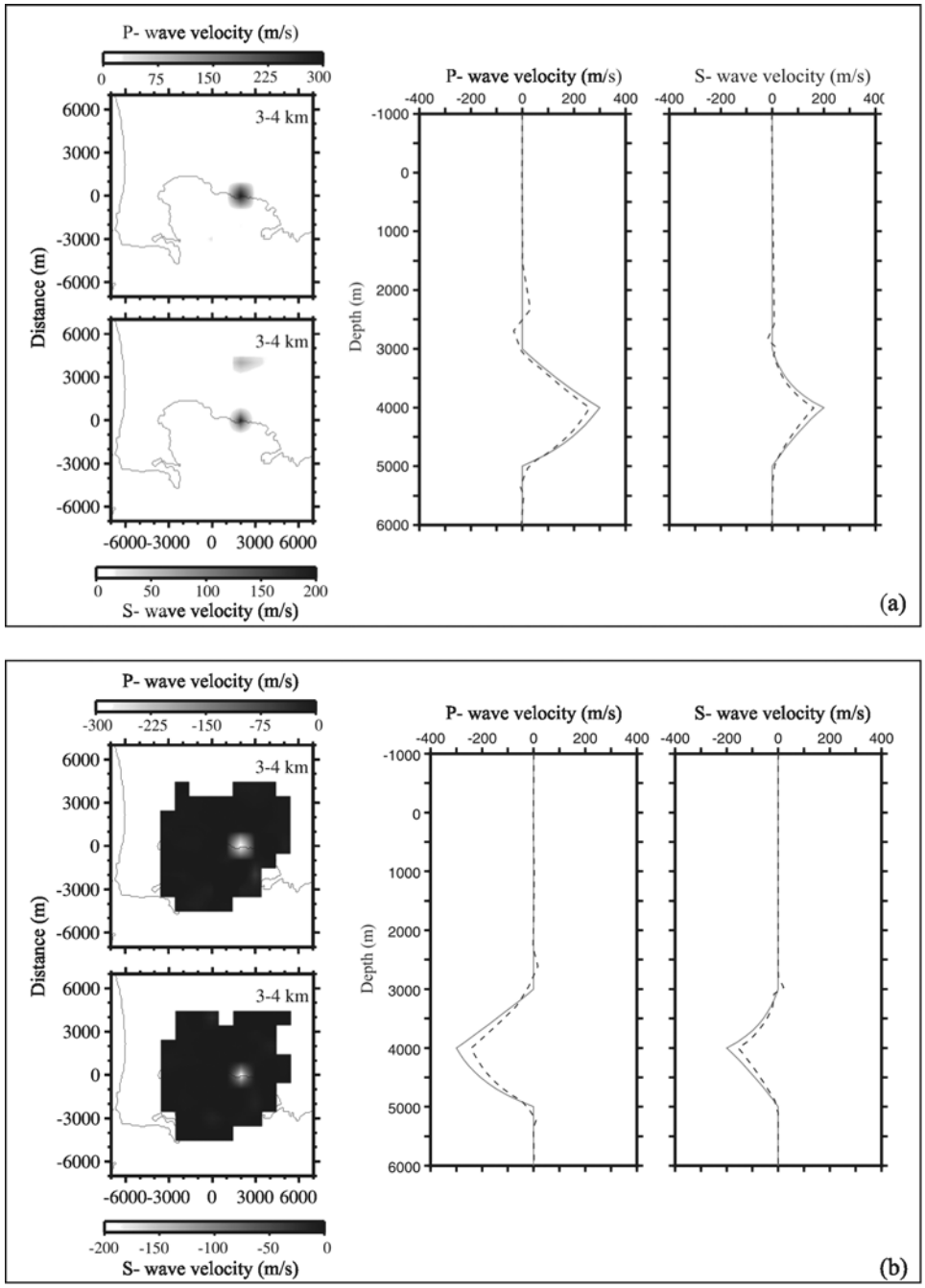

Figure 7. Map views and vertical profiles describing the results of the spike tests for a velocity anomaly located at 4 km depth between the Solfatara and the Accademia areas. Both the results for (a) a positive anomaly and (b) a negative velocity anomaly as well as the comparison between recovered anomalies (dark dashed lines) and initial spike models are shown.

stations could resolve velocity structures satisfactorily, we performed a bootstrap statistics test to determine the uncertainty on velocity values in our final solution.

[26] In general, the best model explaining the observed data set (t_i^{obs}) is described by a finite number of model parameters (Θ) whose calculated travel times (t_i^{cal}) differ from t_i^{obs} by means of time residuals (x_i). Therefore the distribution of time residuals represents a way to estimate the closeness of the observed data distribution to that of true data. However, since the true data distribution is unknown, there is not an objective way to estimate that closeness and hence to be confident in the final model solution. *Aoike et al.* [1998] showed that searching for the most consistent distribution of travel time residuals by bootstrap statistics can be a possible approach to assess the most representative distribution of model parameters and so to evaluate uncertainties in the final best fit velocity model.

[27] We applied a bootstrap statistics approach by generating artificial data sets (e.g., the bootstrap samples)

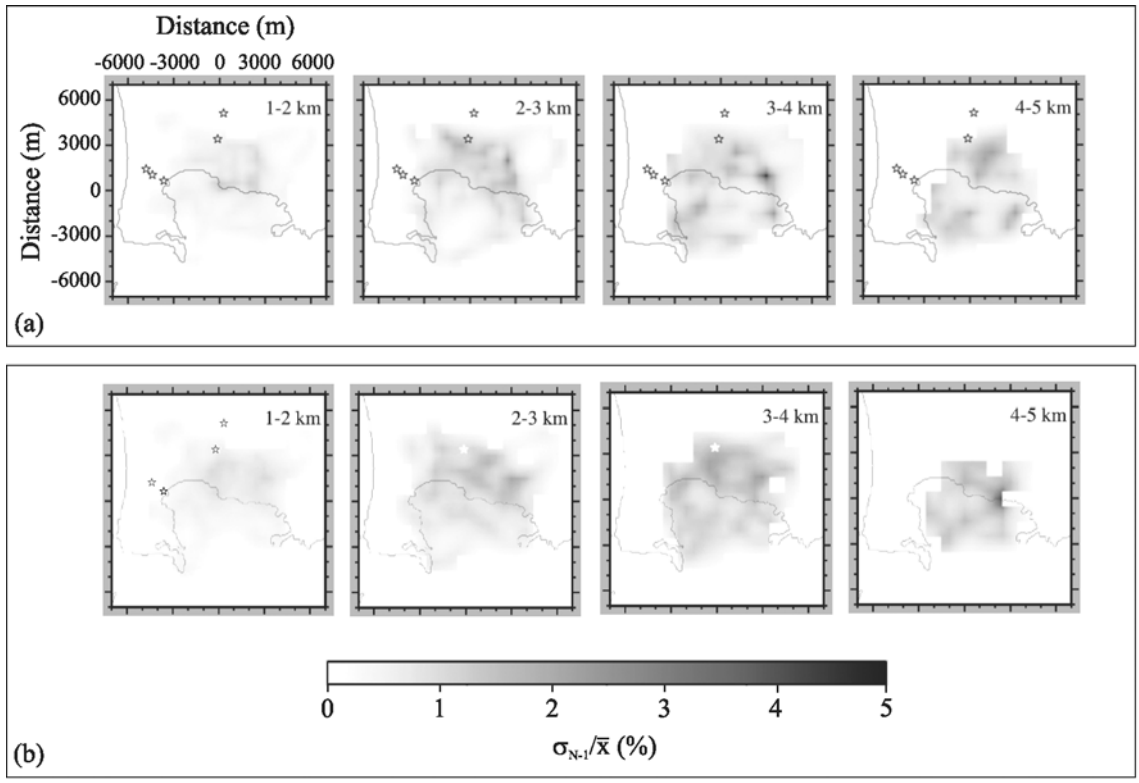

Figure 8. Normalized standard deviation for (a) *P* wave and (b) *S* wave velocity models resulting from bootstrap statistics.

from the distribution of the final model parameters $G(x_i; \Theta)$ which were constituted by as many new time data (t_i*) as the number of observed data. Each bootstrap sample was generated by adding randomly selected residuals x_i to the kth calculated travel time t_k^{cal}. By inverting each bootstrap sample, new model parameters (*Θ) were obtained. The generation of bootstrap samples and the inversion procedure was repeated 1000 times. Both the mean velocity of structures ($\bar{x}$) and the normalized standard deviation ($\sigma_{N-1}/\bar{x}$) was computed for *P* wave and *S* wave velocity models (Figures 8a and 8b). Note that very low uncertainties ($\sigma_{N-1}/\bar{x} \sim 0$) which would imply no perturbation in the initial model, were masked out because they are meaningless. Because of computational limitations we have not performed the complete investigation suggested by *Aoike et al.* [1998], who calculated the Extended Information Criterion (EIC) at each iteration step of the inversion procedure. However, we found that increasing the number of bootstrapped data does not affect the estimation and that the "best" recovered model falls into the confidence interval of the bootstrapped population. Therefore we believe that we obtained a statistical estimation of the *P* wave and *S* wave velocity uncertainties related to each inversion cell.

[28] Figures 8a and 8b show that we found similar normalized uncertainties for both *P* wave and *S* wave velocities models. This is consistent with the similar distribution of *P* time and *S* time residuals since our ray sampling is similar in both cases. This analysis makes us confident that we recovered a realistic *P* wave and *S* wave velocity distribution underneath the CF Caldera.

5. Discussion

5.1. Modeling of Rock Physics Parameters Affecting Seismic Velocities

[29] Many rock physics parameters contribute to changes in seismic velocities of rocks in addition to mineralogy, porosity, and in situ stress conditions such as pore fluid properties, which in turn depend on temperature and pressure [*Birch*, 1960; *Spencer and Nur*, 1976; *O'Connel and Budiansky*, 1974; *Toksoz et al.*, 1976; *Ito et al.*, 1979; *Christensen*, 1985; *Wang and Nur*, 1989; *Sanders et al.*, 1995; *Dvorkin et al.*, 1999b]. It is well known that the content and physical state of fluids affect more strongly *P* wave velocities than *S* wave velocities. It turns out that the V_p/V_s ratio proves useful in discriminating zones saturated with fluids, which in turn also provides insight into their physical state.

[30] Since hydrothermal fluids might play a fundamental role in triggering unrest at CF [*Oliveri del Castillo and Quagliariello*, 1969; *Casertano et al.*, 1976; *Chiodini et al.*, 2003], mechanisms caused by changes in temperature and pressure of fluids have been investigated to constrain the interpretation of V_p/V_s anomalies.

[31] In dry rocks, temperature effects on velocities are smaller than in fluid-saturated rocks. In dry conditions, the decrease in velocities is believed to be due to the softening of the rock matrix and to the increase in porosity which

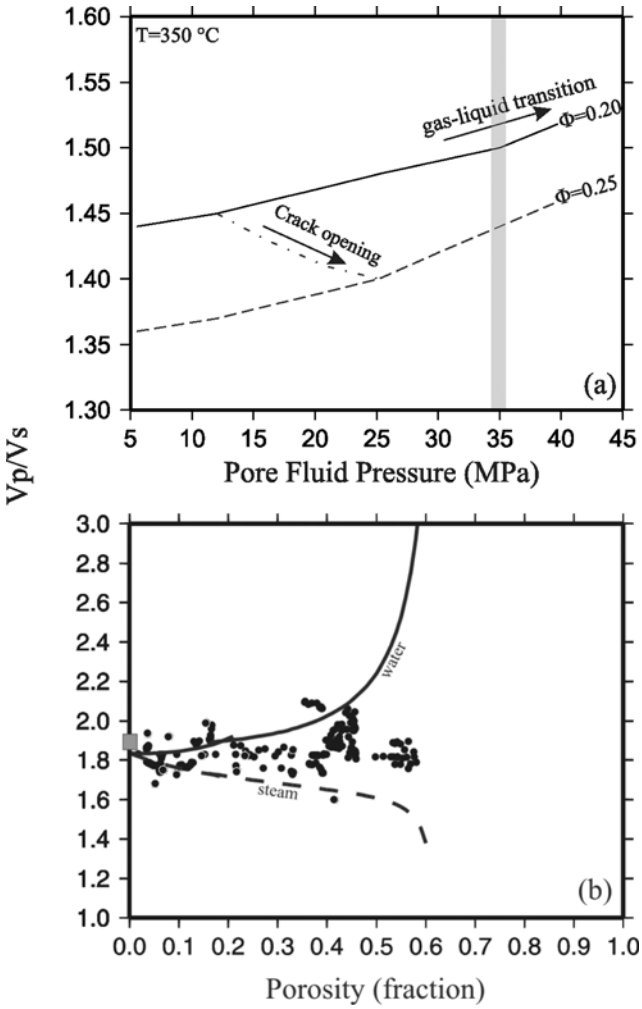

Figure 9. (a) Theoretical modeling of the V_p/V_s ratio as a function of pore pressure in a tuffite at 350°C. (b) Theoretical modeling of the V_p/V_s ratio as a function of porosity computed for both water- and steam-saturated conditions. Laboratory results for site-relevant rocks from *Vanorio et al.* [2002] and *Vanorio* [2003] are shown for comparison. At 0% of porosity the V_p/V_s ratio of minerals forming rocks is reported.

results from the different thermal expansion of minerals [*Kern*, 1982; *Wang and Nur*, 1986]. However, in dry rocks, temperature effects are not so effective until partial melting is reached, which leads V_s to decrease more strongly than V_p [*Sanders et al.*, 1995; *Mavko*, 1980; *Mizutani and Kanamori*, 1964]. This means that increasing temperature mainly decreases the shear modulus of the rock. *Wang* [1988] has explained this phenomenon by a "lubrification" effect: as temperature increases, the rock matrix softens and expands, which makes sliding along grain contacts easier. These effects drive V_p/V_s to increase as temperature increases and, more specifically, to increase to infinity upon melting [*Mizutani and Kanamori*, 1964]. On the other hand, in fluid-saturated rocks, the effect of temperature on pore fluid properties alone enhances the temperature dependence of *P* wave velocity because of changes in fluid compressibility, which are induced by fluid phase transition [*Wang and Nur*, 1989; *Ito et al.*, 1979]. Since such a transition does not affect the shear modulus, and hence *S* wave velocities (i.e., slight *S* wave velocity changes occur because of a density effect), low V_p/V_s ratios characterize gas-bearing rocks (i.e., high fluid compressibility), while higher values of V_p/V_s indicate liquid-bearing formations (i.e., low fluid compressibility). Furthermore, pore fluid pressure may also play a role by inducing a fluid phase transition as well as in keeping pores and cracks open. As a consequence, velocities are further affected. *Dvorkin et al.* [1999b] have shown by laboratory measurements and effective medium modeling that crack opening induced by increasing pore pressure leads V_p/V_s to strongly decrease in gas-bearing rocks.

[32] The variation of *P* wave and *S* wave velocities as a function of pore fluid temperature and pressure has been reported for sandstones and granites under relatively low parts of the temperature and pressure range [*Wang and Nur*, 1989; *Ito et al.*, 1979]. Therefore, for site-relevant rocks (i.e., consolidated tuffites), we theoretically reproduced the effect of higher temperatures and pressures on V_p/V_s via modeling as proposed by *Dvorkin and Nur* [1996]. Since our intention was to model sediments with a nonzero stiffness of the dry matrix, we used the upper Hashin-Shtrikman bound to appropriately model the elastic moduli. Once the moduli and density of the dry matrix are computed (see *Dvorkin and Nur* [1996] and *Dvorkin et al.* [1999a] for details), the computation in the low-frequency domain (i.e., fluid and solid motions are in phase) of the bulk and shear moduli of the saturated sediment come from Gassmann's equation [*Gassmann*, 1951]. In the reported modeling, pore fluid is described by a mixture of water and carbon dioxide (20% of carbon dioxide and 80% of water) whose bulk modulus and density were computed [*Batzle and Wang*, 1992] for a constant temperature of 350°C and by only varying pressure conditions.

[33] Figure 9a shows the result of modeling where the variation of V_p/V_s as a function of $P_{fluid\ pressure}$ is shown for a tuffite having porosity (Φ) equal to 20%. Lithostatic pressure was kept constant at 70 MPa (~4 km depth) and variations of effective pressure (i.e., $P_{\text{lithostatic}} - P_{\text{fluid pressure}}$) was simulated by varying $P_{\text{fluid pressure}}$ from 5 to 45 MPa. Figure 9a shows that for a given rock porosity (Φ = 20%, solid black line in Figure 9a), the increase of pore fluid pressure leads to a decrease in pore fluid compressibility (i.e., vapor-liquid transition is simulated) and, as a consequence, the V_p/V_s ratio increases. Note that for concentrations of CO_2 equal to 20% the binary system H_2O-CO_2 shows a critical point at a temperature of 325°C and pressure of 40 MPa [*Takenouchi and Kennedy*, 1964]. Now, let us assume that increasing pore fluid pressure leads porosity to increase (i.e., crack opening). As an example, Figure 9a also shows the expected variation in V_p/V_s in the case where an increase of pore fluid pressure leads the bulk rock porosity to increase by 5% (Φ = 25%, dashed black line in Figure 9a). The line connecting rock models having different porosity describes the result of computation by slightly increasing porosity by steps of 1%. Figure 9a shows that in gas-bearing rocks, crack opening leads the V_p/V_s ratio to decrease as a function of pore pressure. Our modeling results are in accordance with those from laboratory experiments [*Ito et al.*, 1979] and effective medium modeling [*Dvorkin et al.*, 1999b], and hence they are not

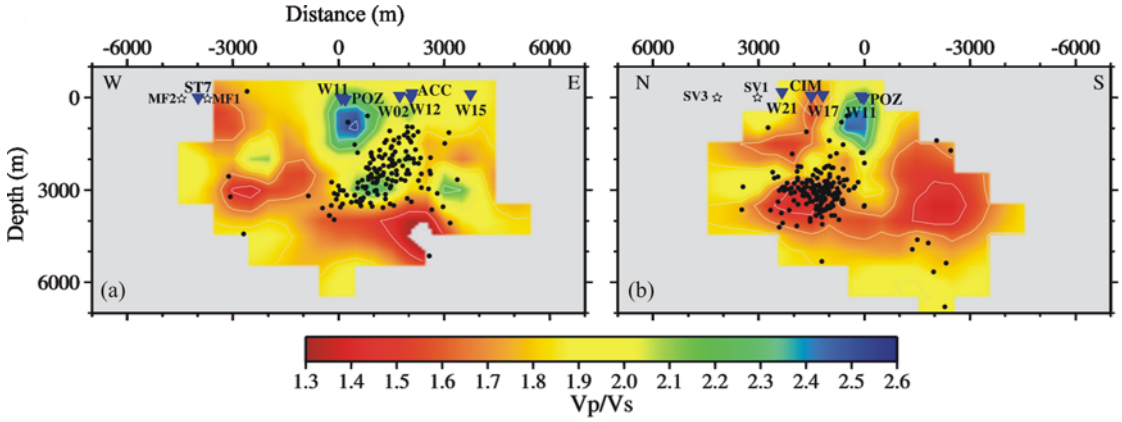

Figure 10. Vertical cross sections describing the variation of the V_p/V_s ratio and earthquake distribution (black points) along the (a) E-W and (b) N-S directions reported in Figure 1. Black stars and triangles indicate well and station locations.

new. However, our results demonstrate that trends are similar at higher pressure and temperature conditions. Our estimates also provide the order of magnitude of V_p/V_s ratios for site-relevant rocks in fully saturated conditions. As input elastic parameters of the rock matrix, we used the mineralogical composition of CF lithologies reported by *Rosi and Sbrana* [1987]. Then, we computed the elastic moduli of the aggregate solid phase from those of the individual mineral constituents by using Hill's formula [*Hill*, 1952]. Furthermore, the availability of laboratory measurements on CF samples [*Vanorio et al.*, 2002; *Vanorio*, 2003] allowed us to further check the validity of input elastic parameters and hence of the modeling results. Figure 9b shows the variation of V_p/V_s as a function of porosity by modeling CF lithologies both in water and steam ($T = 100^{\circ}$C) saturated conditions and simulating ambient pressure conditions ($P_{\text{effective}} = 0$). Figure 9b shows the comparison between the results of modeling and laboratory measurements done on CF samples and well core plugs under dry and ambient pressure conditions [*Vanorio et al.*, 2002; *Vanorio*, 2003]. Laboratory data fall within the two bounds making us confident in the input elastic parameters used for the modeling.

5.2. Deduced V_p/V_s Images at CF

[34] Figures 10a and 10b show the deduced V_p/V_s vertical cross sections along the E-W and N-S directions (Figure 4c). The V_p/V_s images mainly show a centered high V_p/V_s anomaly located at ~1.5 km depth (also noted by *Aster and Meyer* [1988]) surrounded by a low V_p/V_s anomaly which shows a flat feature at 4 km depth beneath the city of Pozzuoli.

[35] In order to compare the retrieved anomalies both in space and depth, we display the vertical velocity profiles extracted from the final 3-D velocity model, for several sites (Figure 11a). Figure 11b describes the variations of V_p, V_s, V_p/V_s and earthquake distribution as functions of depth. Several *P* wave and *S* wave velocity profiles indicate reversal trends (e.g., velocity values decrease with depth) which weaken moving radially away from the center of the caldera (the city of Pozzuoli and Solfatara zone) toward more external sites (Agnano, Arco Felice, Montagna Spaccata-Quarto).

[36] In general, velocity logs going through reversals mark departures of the effective stress from normal compaction trends [*Hottmann and Johnson*, 1965; *Pilkington*, 1988; *Bowers*, 2002]. Overpressure, which can be caused by fluid expansion among other factors, is thought to cause reversals both in *P* wave and *S* wave velocity logs as it prevents the effective stress from increasing as fast as it would under normal hydrostatic or lithostatic pressure conditions. The point indicating the departure of the compaction-dependent physical property (velocity in this case) from its normal trend marks the onset of overpressure [*Bowers*, 2002] and in turn the bottom of the caprock formations. In Figure 11b, the acoustic velocity log of the San Vito well (black line) [*Agip*, 1987] is compared with the velocity profile coming from tomographic inversion. In order to render acoustic velocity at the seismic resolution scale, we scaled the original well log data by averaging velocity [*Backus*, 1962]. There is a fairly good agreement between trends which makes us confident in the inversion results. Figure 11b also shows that *P* wave velocity logs indicate a stronger reversal compared to *S* velocity which, in turn, is ultimately responsible for the decrease in the V_p/V_s ratio. This implies that *P* wave velocity reversals are further enhanced by the presence of gas in addition to that by fracturing. The latter, under the hypothesis of overpressure, affects both *P* wave and *S* wave velocities. Also, histograms mapping earthquake occurrence at depth (Figure 11b) show that earthquakes mainly occur both at the top of reversal trends and within the low V_p/V_s.

[37] On the basis of the results discussed above, we are confident in interpreting the low V_p/V_s anomaly occurring at 4 km depth beneath the center of the caldera and below the reversal velocity zone as evidence of overpressured gas-bearing rocks at supercritical conditions (temperatures of ~400°C were reported in the San Vito well at 3 km depth [*Agip*, 1987]). In contrast, as proposed by *Aster and Meyer* [1988], the shallower higher V_p/V_s anomaly at 1 km suggests the presence of rocks containing brine probably due to steam condensation as a result of lower temperatures measured at shallow depth [*Agip*, 1987].

[38] We emphasize that our results may also provide an explanation for data reported by *Ferrucci et al.* [1992] and

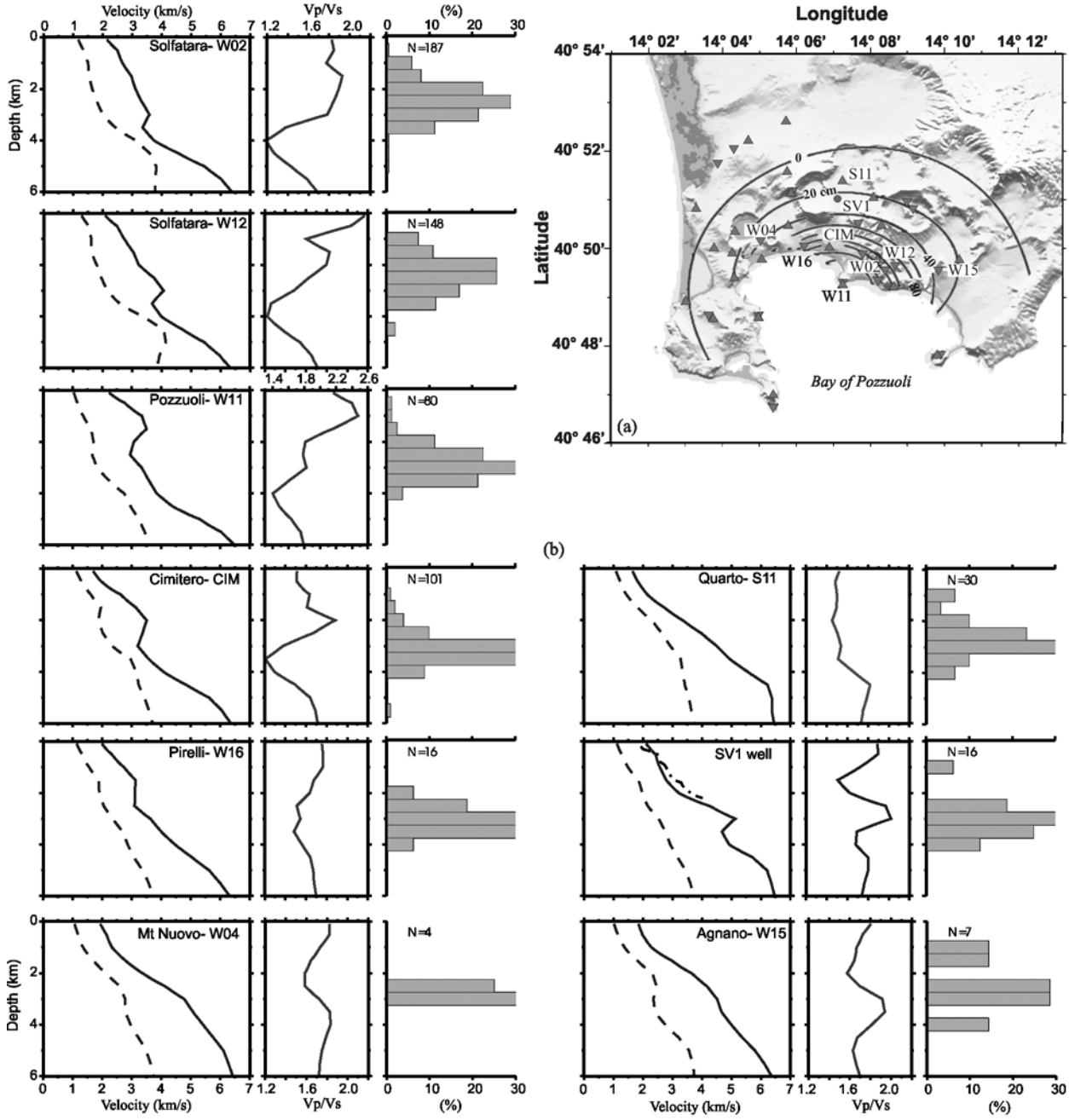

Figure 11. (a) Map view of site locations for the vertical profiles shown in Figure 11b. (b) Velocity logs showing V_p (solid line), V_s (dashed line), and the V_p/V_s ratio (solid line) extracted from the final 3-D velocity models. Earthquake distribution was computed along vertical profiles having an offset equal to 1 km. Dotted line for the SV1 site shows the result obtained by averaging well log data.

De Lorenzo et al. [2001], who interpreted the *P-S* conversion and the low Q_p as being due to the presence of a magmatic reservoir.

[39] The decrease of Q_p for seismic waves has often been interpreted as being a function of temperature. This is supported by laboratory data gathered in the temperature range between 600°C and 1280°C both at seismic (0.1–10 Hz) [*Kampfmann and Berckhemer*, 1985] and at higher frequencies (from 60 kHz to 1 MHz) [*Mizutani and Kanamori*, 1964; *Sato et al.*, 1989; *Sato and Sacks*, 1989]. However, these decreases occur just below the solidus and upon melt formation. In addition, as previously stated, an increase of V_p/V_s to infinity accompanies the Q_p decrease upon melt formation [*Mizutani and Kanamori*, 1964].

[40] On the other hand, at lower temperatures, the variation of Q_p seems to be dominated by mechanisms related to fluid saturation and phase changes [*Bourbié et al.*, 1986]. Decreases of Q_p have been reported in porous rocks as being caused by partial saturation (i.e., gas-liquid mixture) [*Winkler and Nur*, 1979; *Mavko and Nur*, 1979] and by fluids at supercritical temperature [*Ito et al.*, 1979; *DeVilbiss Munoz*, 1980; *Ponko and Sanders*, 1994; *Sanders et al.*,

1995]. Accordingly, *Sanders et al.* [1995] interpreted the low V_p/V_s ratio and the low Q_p inferred from the inversion of microearthquake travel times in the Long Valley Caldera as being due to the presence of rocks containing gas. Therefore we argue that both the low Q_p reported by *De Lorenzo et al.* [2001] beneath the CF Caldera and the low V_p/V_s ratio reported in this study document the presence of cracked rocks containing supercritical fluids below 3 km. Furthermore, a correlation between a low V_p/V_s ratio and *P-S* converted phases has been reported by *Cerda* [2001] in the Teal South Field, Gulf of Mexico. Yet, results constrained by well data documented the presence of gas formations as being responsible for the above mentioned signatures. We emphasize that in the Bay of Pozzuoli, *Ranieri and Mirabile* [1991] reported discontinuous high-amplitude reflectors on seismic reflection lines at ~3.5 km depth which locally show bright spot features.

6. Conclusions

[41] At shallow depth, we found similar velocity trends to those reported in the previous tomographic study of *Aster and Meyer* [1988]. However, our augmented database allowed an improved resolution of the tomographic images at depths between 4 km and 5 km where we found an anomalously low V_p/V_s ratio.

[42] The retrieved V_p/V_s anomalies at CF were interpreted by effective medium modeling for site-relevant rocks and were compared with previous studies [*Ito et al.*, 1979; *Dvorkin et al.*, 1999b] to investigate the role of mechanisms related both to the gas/liquid transition and to overpressured fluids. Modeling of rock physical properties as well as the reversal trends encountered along velocity profiles led us to interpret the low V_p/V_s anomaly at 4 km depth as the top of formations enriched in gas under supercritical conditions. Reversal trends gather in the center of the caldera and imply a localized pressure source as suggested by the narrow-bell shape of the recorded displacement (see the map view of the recorded uplift in Figures 1 and 11a). The signature of a low V_p/V_s ratio at 4 km depth excludes the presence of melted rocks at 4 km as such a presence would require high V_p/V_s ratios. The absence of melt formations down to 4–5 km depth is also in accordance with the results reported by *Zollo et al.* [2003].

[43] The analyzed data set of the 1982–1984 crisis showed that earthquake locations are mostly distributed on the top of velocity reversals and within the low V_p/V_s anomaly. Since these signatures were interpreted as being caused by gas under supercritical conditions, we speculate that seismicity might be induced by overpressured fluids. However, no specific seismicity analysis were made with regard to this issue. Nevertheless, a phenomenological correlation among (1) uplift rate, (2) seismicity and (3) increase of the H_2O/CO_2 ratio in fumaroles as a function of time is noted in the CF Caldera [*Chiodini et al.*, 2001, 2003]. Such a correlation suggests that the observed phenomena may have a common origin.

[44] Episodical self-sealing processes inducing transient fluid pressure effects may represent significant mechanisms in inflating calderas. *Batzle and Simmons* [1977] emphasize that hydrothermal systems are active environments where permeability destruction due to mineral precipitation, crack healing, and sealing competes with permeability creation due to the fracturing processes. Permeability destruction may even overwhelm crack creation by rapidly generating caprock formations through these hydrothermal self-sealing processes [*Facca and Tonani*, 1967]. Furthermore, theoretical modeling [*Sleep and Blanpied*, 1994] showed that both the creation of microcracks during earthquakes in hydraulically clogged fault zones and the following compaction, might lead to cycles of high pore fluid pressure along faults. These results support models which have been proposed to describe the hydromechanical behavior of fault zones, namely the fault valve model [*Sibson*, 1992].

[45] A correlation between earthquake swarms, low V_p/V_s anomalies and CO_2 emissions is also known from other calderas, such as Long Valley Caldera [*Farrar et al.*, 1995; *Sanders et al.*, 1995; *Hill et al.*, 1990] and Yellowstone [*Husen et al.*, 2004]. In the CF Caldera, the gas origin (e.g., deep flooding or in situ production), as well as the mechanisms responsible for their storage and the consequent overpressure, still remain open questions and hence a matter of speculation. However, the presence of self-sealing processes in the CF Caldera [*Chelini*, 1984] which are fast enough at hydrothermal conditions [*Smith and Evans*, 1984; *Summers et al.*, 1978] might account for fluid pressure generation. Regarding the origin of gas, an enhanced flooding of fluids caused by degassing from a deeper magmatic reservoir has been suggested by *Chiodini et al.* [2003]. However, we emphasize that CO_2 production promoted by decarbonation reactions [*D'Amico et al.*, 1987; *Rosi and Sbrana*, 1987] which occur in carbonate rocks under high temperatures ($T \geq 300°C$) may be as likely. The evidence of a carbonatic basement reported by *Zollo et al.* [2003] as well as the recovery at ~3000 m depth within the thermometamorphic basement of tuffites having a carbonatic matrix [*Chelini*, 1984], might support this hypothesis.

[46] Our results from the CF Caldera show strong similarities with those reported in other volcanic areas suggesting that storage of supercritical fluids at depth has to be tracked to monitor the caldera activity and to prevent risks.

[47] With respect to the future state of activity in the CF Caldera and on the basis of fluid-induced seismicity, the progress of seismic tools in characterizing reservoirs makes a strong case for time lapse tomography in this active volcanic area in order to track gas front movements and to monitor flooding processes coming from deeper sources.

[48] **Acknowledgments.** This work was supported by the Gruppo Nazionale di Vulcanologia and Dipartimento della Protezione Civile - SERAPIS Project (Seismic Reflection Acquisition Project for Imaging Structures) (FP2000-2003). The European Community sponsored T. Vanorio under the Marie Curie-IHP program (HPMF-CT-2002-01342). We also appreciated the thoughtful comments and suggestions of the anonymous reviewers who helped us to improve the manuscript.

References

Agip (1987), Geologia e geofisica del sistema geotermico dei Campi Flegrei, internal Report, 17 pp., Milan, Italy.

Allard, P., A. Maiorani, A. Tedesco, G. Cortecci, and B. Turi (1991), Isotopic study of the origin of sulfur and carbon in Solfatara fumaroles, Campi Flegrei caldera, *J. Volcanol. Geotherm. Res.*, *48*, 139–159.

Aoike, K., O. Nishizawa, and T. Sato (1998), Application of the Extended Information Criterion to Seismic Tomography using Local earthquakes, paper presented at 4th SEGJ International Symposium, Soc. of Explor. Geophys. of Jpn., Tokyo.

Aster, R. C., and R. P. Meyer (1988), Three-dimensional velocity structure and hypocenter distribution in the Campi Flegrei caldera, Italy, *Tectonophysics*, *149*, 195–218.

Backus, G. F. (1962), Long-wave elastic anisotropy produced by horizontal layering, *J. Geophys. Res.*, *67*, 4427–4441.

Barberi, F., G. Corrado, F. Innocenti, and G. Luongo (1984), Phlegraen Fields 1982–1984: Brief chronicle of a volcano emergency in a sensely populated area, *Bull. Volcanol.*, *47*, 175–185.

Batzle, M. L., and G. Simmons (1977), Geothermal systems: Rocks, fluids, fractures, in *The Earth's Crust: Its Nature and Physical Properties*, *Geophys. Monogr. Ser.*, vol. 20, edited by J. C. Heacock, pp. 233–242, AGU, Washington, D. C.

Batzle, M. L., and Z. W. Wang (1992), Seismic properties of pore fluids, *Geophysics*, *57*, 1396–1408.

Benz, H. M., B. A. Chouet, P. B. Dawson, J. C. Lahr, R. A. Page, and J. A. Hole (1996), Three-dimensional *P* and *S* wave velocity structure of Redoubt Volcano, Alaska, *J. Geophys. Res.*, *101*, 8111–8128.

Bianchi, R., A. Coradini, C. Federico, G. Giberti, P. Lanciano, J. P. Pozzi, G. Sartoris, and R. Scandone (1987), Modeling of surface deformations in volcanic areas: The 1970–1972 and 1982–1984 crises at Campi Flegrei, Italy, *J. Geophys. Res.*, *92*, 14,139–14,150.

Birch, F. (1960), The velocity of compressional waves in rocks to 10 kbars, part 1, *J. Geophys. Res.*, *65*, 1083–1102.

Bonafede, M. (1991), Hot fluid migration: An efficient source of ground deformation: Application to the 1982–1985 crisis at Campi Flegrei-Italy, *J. Volcanol. Geotherm. Res.*, *48*, 187–198.

Bonafede, M., M. Dragoni, and F. Quareni (1986), Displacement and stress field produced by a centre of dilation and by a pressure source in a viscoelastic half-space: Application to the study of ground deformation and seismic activity at Campi Flegrei, *Geophys. J. R. Astron. Soc.*, *87*, 455–485.

Bourbié, T., O. Coussy, and B. Zinszner (1986), *Acoustic of Porous Media*, 334 pp., Technip, Paris.

Bowers, G. L. (2002), Detecting high overpressure, *Leading Edge*, *21*, 174–177.

Capuano, P., and U. Achauer (2003), Gravity field modeling in the Vesuvius and campanian area, in *The TomoVes Seismic Project: Looking Inside Mt. Vesuvius*, edited by A. Zollo et al., Cuen, Naples, Italy.

Casertano, L., A. Oliveri, and M. T. Quagliariello (1976), Hydrodynamics and geodynamics in the Phlegraean Fields area of Italy, *Nature*, *264*, 161–164.

Cerda, F. A. (2001), Time-lapse (4-D), V_p/V_s interpretation of reservoir depletion in Teal South Field, Gulf of Mexico, Ph.D. thesis, 93 pp., Univ. of Tex. at Austin, Austin.

Chelini, W. (1984), Alcuni Aspetti Geologici-Petrografici sul Sistema Geotermico Flegreo, *Rend. Soc. It. Miner. Petrol.*, *39*, 387–391.

Chiodini, G., F. Frondini, C. Cardellini, D. Granieri, L. Marini, and G. Ventura (2001), CO_2 degassing and energy release at Solfatara Volcano, Campi Flegrei, Italy, *J. Geophys. Res.*, *106*, 16,213–16,221.

Chiodini, G., M. Todesco, S. Caliro, C. Del Gaudio, G. Macedonio, and M. Russo (2003), Magma degassing as a trigger of bradyseismic events: The case of Phlegrean Fields (Italy), *Geophys. Res. Lett.*, *30*(8), 1434, doi:10.1029/2002GL016790.

Christensen, N. I. (1985), Measurement of dynamic properties of rock at elevated temperatures and pressures, *ASTM Spec. Tech. Publ.*, *869*, 93–107.

D'Amico, C., F. Innocenti, and F. P. Sassi (1987), *Magamatismo e Metamorfismo*, 536 pp., Utet Ed., Torino, Italy.

De Lorenzo, S., A. Zollo, and F. Mongelli (2001), Source parameters and 3-D attenuation structure from the inversion of microearthquake pulse width data: *Qp* imaging and inferences on the thermal state of the Campi Flegrei Caldera, *J. Geophys. Res.*, *106*, 16,265–16,286.

De Natale, G., and A. Zollo (1986), Statistical analysis and clustering features of the Phlegraean Fields earthquake sequence, *Bull. Seismol. Soc. Am.*, *76*(3), 801–814.

De Natale, G., F. Pingue, P. Allarde, and A. Zollo (1991), Geophysical and geochemical modelling of the 1982–1984 unrest phenomena at Campi Flegrei caldera (southern Italy), *J. Volcanol. Geotherm. Res.*, *48*, 199–222.

DeVilbiss Munoz, J. W. (1980), Wave dispersion and absorption in partially saturated rocks, Ph.D. thesis, Stanford Univ., Stanford, Calif.

Dvorak, J. J., and P. Gasparini (1991), History of earthquakes and vertical ground movement in Campi Flegrei caldera, southern Italy: Comparison of precursory event to the A.D. eruption of Monte Nuovo and activity since 1968, *J. Volcanol. Geotherm. Res.*, *48*, 77–92.

Dvorkin, J., and A. Nur (1996), Elasticity of high-porosity sandstones: Theory for two North Sea datasets, *Geophysics*, *61*, 1363–1370.

Dvorkin, J., M. Prasad, A. Sakai, and D. Lavoie (1999a), Elasticity of marine sediments: Rock physics modeling, *Geophys. Res. Lett.*, *26*, 1781–1784.

Dvorkin, J., G. Mavko, and A. Nur (1999b), Overpressure detection from compressional- and shear-wave data, *Geophys. Res. Lett.*, *26*, 3417–3420.

Dzurisin, D., and K. Yamashita (1987), Vertical surface displacements at Yellowstone caldera, Wyoming, 1976–1986, *J. Geophys. Res.*, *92*, 13,753–13,766.

Facca, G., and F. Tonani (1967), The self-sealing geothermal field, *Bull. Volcanol.*, *30*, 271–273.

Farrar, C. D., M. L. Sorey, W. C. Evans, J. F. Howle, B. D. Kerr, B. M. Kennedy, C. Y. King, and J. R. Southon (1995), Forest-killing diffuse CO_2 emission at Mammoth Mountain as a sign of magmatic unrest, *Nature*, *376*, 675–678.

Ferrucci, F., A. Hirn, J. Virieux, G. De Natale, and L. Mirabile (1992), *P-SV* conversions at a shallow boundary beneath Campi Flegrei Caldera (Naples, Italy): Evidence for the magma chamber, *J. Geophys. Res.*, *97*, 15,351–15,359.

Gaeta, F. S., G. De Natale, F. Peluso, D. Castagnolo, C. Troise, F. Pingue, D. G. Mita, and S. Rossano (1998), Genesis and evolution of unrest episodes at Campi Flegrei caldera: The role of the thermal fluid dynamical processes in the geothermal system, *J. Geophys. Res.*, *103*, 20,921–20,933.

Gassmann, F. (1951), Elastic wave through a packing of spheres, *Geophysics*, *16*, 673–685.

Hill, D. P., W. L. Ellsworth, M. J. S. Johnston, J. O. Langbein, D. H. Oppenheimer, A. M. Pitt, P. A. Reasenberg, M. L. Sorey, and S. R. McNutt (1990), The 1989 earthquake swarm beneath Mammoth Mountain, California: An initial look at the 4 May through 30 September activity, *Bull. Seismol. Soc. Am.*, *80*, 325–339.

Hill, R. (1952), The elastic behavior of crystalline aggregate, *Proc. Phys. Soc. London, Ser. A*, *65*, 349–354.

Hole, J. A., T. M. Brocher, S. L. Klemperer, T. Parsons, H. M. Benz, and K. P. Furlong (2000), Three-dimensional seismic velocity structure of the San Francisco Bay area, *J. Geophys. Res.*, *105*, 13,859–13,874.

Hottmann, C. E., and R. K. Johnson (1965), Estimation of formation pressures from log-derived shale properties, *Soc. Pet. Technol.*, *17*, 717–722.

Husen, S., R. B. Smith, and G. P. Waite (2004), Evidence for gas and magmatic sources beneath the Yellowstone volcanic field from seismic tomographic imaging, *J. Volcanol. Geotherm. Res.*, *131*, 397–410.

Ito, H., J. DeVilbiss, and A. Nur (1979), Compressional and shear waves in saturated rock during water-steam transition, *J. Geophys. Res.*, *84*, 4731–4735.

Kampfmann, W., and H. Berckhemer (1985), High temperature experiments on the elastic and anelastic behavior of magmatic rocks, *Phys. Earth Planet. Inter.*, *40*, 223–247.

Kern, H. (1982), Elastic wave velocity in crustal and mantle rocks at high pressure and temperature: The role of the high-low quartz transition and of dehydration reactions, *Phys. Earth Planet. Inter.*, *29*, 12–23.

Kissling, E., W. L. Ellsworth, D. Eberhart-Phillips, and U. Kradolfer (1994), Initial reference models in local earthquake tomography, *J. Geophys. Res.*, *99*, 19,635–19,646.

Latorre, D., J. Virieux, T. Monfret, V. Monteiller, T. Vanorio, J.-L. Got, and H. Lyon-Caen (2004), A new seismic tomography of Aigion area (Gulf of Corinth-Greece) from a 1991 dataset, *Geophys. J. Int.*, *159*, 1013–1031.

Lay, T., and T. C. Wallace (1995), *Modern Global Seismology*, pp. 218–219, Springer, New York.

Le Meur, H., J. Virieux, and P. Podvin (1997), Seismic tomography of the Gulf of Corinth: A comparison of methods, *Ann. Geophys*, *40*, 1–25.

Mavko, G. (1980), Velocity and attenuation in partially molten rocks, *J. Geophys. Res.*, *85*, 5173–5189.

Mavko, G., and A. Nur (1979), Wave attenuation in partially saturated rocks, *Geophysics*, *44*, 161–178.

Menke, W. (1984), *Geophysical Data Analysis: Discrete Inverse Theory*, 260 pp., Springer, New York.

Mizutani, H., and H. Kanamori (1964), Variation of elastic wave velocity and attenuation property near the melting temperature, *J. Phys. Earth*, *12*, 43–49.

Newhall, C. G., and D. Dzurisin (1988), Historical unrest at large calderas of the world, *U.S. Geol. Surv. Bull. B*, *1855*(1–2), 1108 pp.

O'Connel, R., and B. Budiansky (1974), Seismic velocities in dry and saturated cracked solids, *J. Geophys. Res.*, *79*, 5412–5426.

Oliveri del Castillo, A., and M. T. Quagliariello (1969), Sulla genesi del bradisismo flegreo, *Atti Assoc. Geofis. Ital.*, *4*, 1–4.

Osservatorio Vesuviano (1985), Bradisismo Flegreo rapporto di Sorveglianza, Gennaio 1982–Gennaio 1984, internal report, Naples, Italy.

Paige, C. C., and M. A. Saunders (1982), LSQR: An algorithm for sparse linear equations and sparse least squares, *Trans. Math. Software*, *8*, 43–71.

Pavlis, H. G., and J. R. Booker (1980), The mixed discrete-continuous inverse problem: Application to the simultaneous determination of earthquake hypocenters and velocity structure, *J. Geophys. Res.*, *85*, 4801–4810.

Pilkington, P. E. (1988), Uses of pressure and temperature data in exploration and new developments in overpressure detection, *Soc. Pet. Technol.*, *40*, 543–549.

Podvin, P., and I. Lecomte (1991), Finite difference computation of traveltimes in very contrasted velocity models: A massively parallel approach and its associated tools, *Geophys. J. Int.*, *105*, 271–284.

Ponko, S. C., and C. O. Sanders (1994), Inversion for *P* and *S* wave differential attenuation structure, Long Valley Caldera, California, *J. Geophys. Res.*, *99*, 2619–2635.

Ranieri, G., and L. Mirabile (1991), Ricerca ed Applicazione di Metodi Geofisici al Rilievo Sperimentale della Struttura Medio-Profonda dell'area Flegrea con uso di Sorgenti Sismiche Water-Gun, *Ann. Ist. Univ. Navale Napoli*, *57*, 149–186.

Rosi, M., and A. Sbrana (Eds.) (1987), Phlegraean Fields, *Quad. Ric. Sci.*, *114*(9), 175 pp.

Sanders, C. O., S. C. Ponko, L. D. Nixon, and E. A. Schwartz (1995), Seismological evidence for magmatic and hydrothermal structure in Long Valley caldera from local earthquake attenuation and velocity tomography, *J. Geophys. Res.*, *100*, 8311–8326.

Sato, H., and I. S. Sacks (1989), Anelasticity and thermal structure of the oceanic upper mantle: Temperature calibration with heat flow data, *J. Geophys. Res.*, *94*, 5705–5715.

Sato, H., I. S. Sacks, and T. Murase (1989), The use of laboratory velocity data for estimating temperature and partial melt fraction in the low-velocity zone: Comparison with heat flow and electrical conductivity studies, *J. Geophys. Res.*, *94*, 5689–5704.

Scandone, R., F. Bellucci, L. Lirer, and G. Rolandi (1991), The Structure of the Campanian Plain and the activity of the Neapolitan volcanoes (Italy), *J. Volcanol. Geotherm. Res.*, *48*, 1–49.

Sibson, R. H. (1992), Implication of fault valve behavior for rupture nucleation and recurrence, *Tectonophysics*, *211*, 283–293.

Sleep, N. H., and T. Blanpied (1994), Ductile creep and compaction: A mechanism for transiently increasing fluid pressure in mostly sealed fault zones, *Pure Appl. Geophys.*, *143*, 9–40.

Smith, D. L., and B. Evans (1984), Diffusional crack healing in quartz, *J. Geophys. Res.*, *89*, 4125–4135.

Spakman, W., and G. Nolet (1988), Imaging algorithms, accuracy and resolution, in *Mathematical Geophysics*, edited by N. Vlaar, pp. 155–187, Springer, New York.

Spencer, C. P., and D. Gubbins (1980), Travel-time inversion for simultaneous earthquake location and velocity structure determination in laterally varying media, *Geophys. J. R. Astron. Soc.*, *60*, 95–116.

Spencer, J. W., Jr., and A. Nur (1976), The effects of pressure, temperature and pore water on velocities in Westerly granite, *J. Geophys. Res.*, *81*, 899–904.

Summers, R., K. Winkler, and J. Byerlee (1978), Permeability changes during the flow of water through Westerly Granite at temperatures of 100°–400°C, *J. Geophys. Res.*, *83*, 339–344.

Takenouchi, S., and G. Kennedy (1964), The binary system H_2O-CO_2 at high temperatures and pressures, *Am. J. Sci.*, *262*, 1055–1074.

Tedesco, D., P. Allard, Y. Sano, H. Wakita, and R. Pece (1990), Helium-3 in subaerial and submarine fumaroles of Campi Flegrei caldera, Italy, *Geochim. Cosmochim. Acta*, *54*, 1105–1116.

Thurber, C. H. (1992), Hypocenter-velocity structure coupling in local earthquake tomography, *Phys. Earth Planet. Inter.*, *75*, 55–62.

Toksoz, M. N., C. H. Cheng, and A. Timur (1976), Velocities of seismic waves in porous rocks, *Geophysics*, *41*, 621–645.

Vanorio, T. (2003), Rocks physics properties of the Campanian Plain, in *The Internal Structure of Mt. Vesuvius: A Seismic Tomography Investigation* [CD-ROM], edited by P. Capuano et al., pp. 553–579, Liguori, Naples, Italy.

Vanorio, T., M. Prasad, A. Nur, and D. Patella (2002), Ultrasonic velocity measurements in volcanic rocks: Correlation with microtexture, *Geophys. J. Int.*, *149*, 22–36.

Wang, Z. W. (1988), Wave velocities in hydrocarbons and hydrocarbon saturated rocks—With applications to EOR monitoring, Ph.D. thesis, Stanford Univ., Stanford, Calif.

Wang, Z. W., and A. Nur (1986), Effect of temperature on wave velocities in sandstones and sand with heavy hydrocarbons, paper presented at 56th Annual Meeting and Exposition, Soc. of Explor. Geophys., Houston, Tex.

Wang, Z. W., and A. Nur (1989), Effect of CO_2 flooding on wave velocities in rocks and hydrocarbons, *Soc. Pet. Eng. Res. Eng.*, *3*, 429–439.

Winkler, K. W., and A. Nur (1979), Pore fluids and seismic attenuation in rocks, *Geophys. Res. Lett.*, *6*, 1–4.

Zollo, A., et al. (2003), Evidence for the buried rim of Campi Flegrei caldera from 3-d active seismic imaging, *Geophys. Res. Lett.*, *30*(19), 2002, doi:10.1029/2003GL018173.

P. Capuano, Dipartimento di Scienze e Tecnologie per l'Ambiente ed il Territorial, Università del Moliere, Via de Gasperi, I-86100 Campobasso, Italy.

G. Russo, Dipartimento di Scienze Fisiche, Università di Napoli Federico II, Viale Cintia, I-80126 Naples, Italy.

T. Vanorio and J. Virieux, UMR-Geosciences Azur, CNRS, Université de Nice, Sophia Antipolis, 250 Rue Albert Einstein, F-06560 Valbonne, France. (vanorio@geoazur.unice.it)